

Tungsten Boride: a 2D Multiple Dirac Semimetal for Hydrogen Evolution Reaction

Aizhu Wang^{1,2}, Lei Shen³, Mingwen Zhao^{4*}, Junru Wang⁴, Weifeng Li⁴, Weijia Zhou¹,
Yuanping Feng^{5*}, and Hong Liu^{1,6*}

¹*Institute for Advanced Interdisciplinary Research, University of Jinan, Jinan, Shandong, 250022, China*

²*Department of Electrical and Computer Engineering and Department of Physics, National University of Singapore, Singapore, 117579, Singapore*

³*Department of Mechanical Engineering, Engineering Science Programme, Faculty of Engineering, National University of Singapore, Singapore, 117575, Singapore*

⁴*School of Physics and State Key Laboratory of Crystal Materials, Shandong University, Jinan 250100, Shandong, China*

⁵*Department of Physics & Centre for Advanced Two-dimensional Materials, National University of Singapore, Singapore, 117542, Singapore*

⁶*State Key Laboratory of Crystal Materials, Shandong University, Jinan, 250100, Shandong, China*

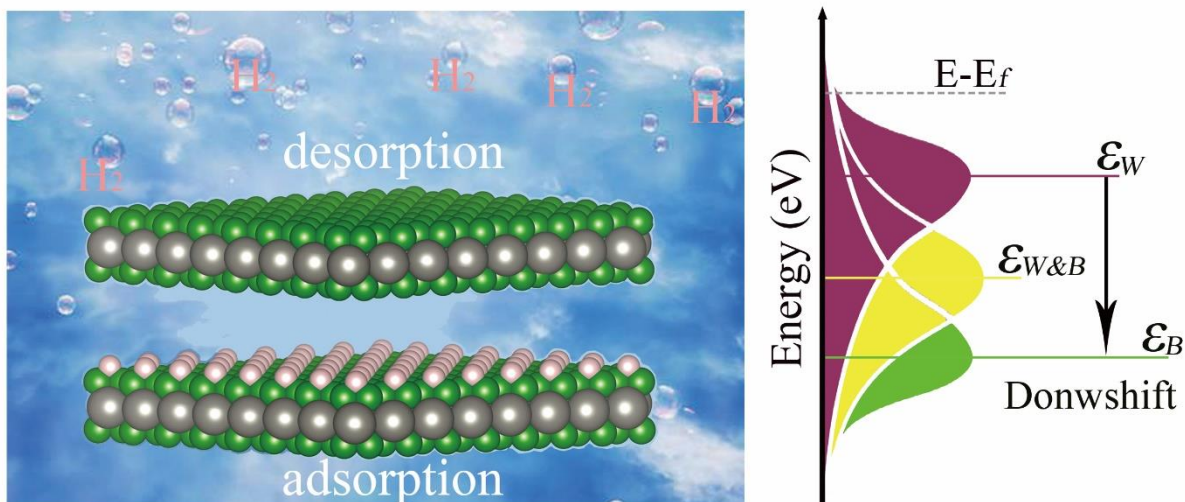
*Correspondences:

zmw@sdu.edu.cn (M. Z.)

phyfyp@nus.edu.sg (Y. F.)

hongliu@sdu.edu.cn (H. L.)

TOC



HIGHLIGHTS

2D WB₄ is first theoretical studied as an efficient electrocatalyst for hydrogen evolution reaction.

The 2D “sandwich” B-W-B lattice intrinsically possesses multiple Dirac states for facilitating the transmission of electrons.

The optimized catalyst shows an ultralow overpotential to realize its ideal catalytic characteristics.

The *d* band center regulated by the *p*-orbitals of borophene subunits is the main driving force for achieving higher activity.

High Pt-like HER activity of the host is essential to offer a guiding principle for discovering optimal noble-metal-free catalysts.

SUMMARY

Here, we propose a two-dimensional (2D) tungsten boride (WB_4) lattice, with the Gibbs free energy for the adsorption of atomic hydrogen (ΔG_{H}) tending to be the ideal value (0 eV) at 3% strained state, to host a better hydrogen evolution reaction (HER) activity. Based on first-principles calculations, it is demonstrated that the multiple d - p - π and d - p - σ Dirac conjugations of WB_4 lattice ensures its excellent electronic transport characteristics. Meanwhile, coupling with the d -orbitals of W, the p -orbitals of borophene subunits in WB_4 lattice can modulate the d band center to get a good HER performance. Our results not only provide a versatile platform for hosting multiple Dirac semimetal states with a “sandwich” configuration, but also offer a guiding principle for discovering the relationship between intrinsic properties of the active center and the catalytic activity of metal layer from the emerging field of 2D noble-metal-free lattices.

Context & Scale

Efficient hydrogen production (H_2) from water could potentially lead to a clean and renewable energy system. Electrochemical water splitting to produce H_2 offers a reliable and sustainable solution for this purpose. The catalysts are important components of water electrolysis cells and largely govern their performance. Considering the high price and limited world-wide supply of Pt-based HER catalysts, the development of non-noble-metal and high activity hydrogen-producing catalysts plays a central role in the current research progress.

In this work, we propose a 2D WB_4 lattice, with the ΔG_H tending to be the ideal value (0 eV) at 3% strained state, host a better HER activity than that in Pt ($\Delta G_H \sim -0.05$ eV). Based on first-principles calculations, we present a systematic theoretical study for the WB_4 lattice with special emphasis on the configuration design and electronic structure, and find that the WB_4 lattice spawns multiple Dirac cones around the Fermi level with considerable fermi velocities to transfer electrons in all directions throughout its structure. Importantly, together with the d -orbitals of W, the p -orbitals of borophene subunits in WB_4 lattice can modulate the d band center to get a good HER performance by regulating external stress. This work provides new insight into the rational design and manipulation of 2D catalysts toward electrochemical hydrogen production and other electroreduction reactions with high selectivity.

INTRODUCTION

When powered by renewable energy sources, the generation of hydrogen from the electrolysis of water is a means to produce a high-energy density, mobile energy carrier without any associated carbon dioxide emissions [1]. At low temperatures, this process can take place in a series of electrochemical devices, ranging from high-current-density polymer electrolyte membrane electrolyzers [2-4] to low-current-density, solar-driven photoelectrochemical cells [5-7]. For all those water-splitting applications, the choice of the hydrogen evolution reaction (HER) catalyst employed at the cathode can have a profound influence on the cost, lifetime, and efficiency of the device. Pt is a very active and commonly used HER catalyst, but its high price and limited worldwide supply [1, 8] make its use a barrier to mass production of H₂ by water electrolysis.

The effective approach to overcome the challenges associated with Pt HER catalysts is to increase the surface to bulk atomic ratio of Pt, thus allowing for a lower metal loading to be used without compromising electrolysis efficiency [1]. Many efforts have really been devoted both experimentally and theoretically in the past few years. For example, chemical treatments [9-11], such as surface modification, alloying, heteroatom doping and so on. Another approach that works is completely replacing Pt with alternative non-Pt catalysts. Such as transition metal alloys, sulfides, carbides, nitrides, and borides, *etc.* [12-16]. Hence, a prerequisite is gaining detailed knowledge of structure-activity correlations for electrode materials to better understand the activity trends and then rapidly discovering new advanced catalysts for HER.

Sitting around carbon in the periodic table, boron is a magic element in the sense that it not only can bond both covalently and ionically [17], but it is capable of forming a great variety of pure allotropes ranging from zero-dimensional clusters to three-dimensional (3D) bulk materials [18-21], suggesting that boron share many of the characteristic of carbon. Advanced research demonstrated that several 3D boride compounds consists of two-dimensional (2D) boron layers as subunits (known as borophene subunits), have recently emerged as a potential new frontier for searching better HER catalysts [22-24], which can be contributed as the strongly bound of borophene subunits within the solid in contrast to the weakly bound graphene layer in graphite. However, the research on the HER activity of 2D borophene subunits is still a blank.

Here, the 2D tungsten boride (WB_4) lattice (**Figure 1(a)**) is proposed, in which a triangular tungsten layer is sandwiched by two borophene subunits, forming a “sandwich” layer. Based on first-principles calculations, we find that the WB_4 lattice has superior stability and multiple Dirac cones due to the d - p - π and d - p - σ conjugations. Moreover, our study demonstrates a different principle to spur HER activity that can go beyond local site optimization by manipulating the d band center within a certain strain range, as evidenced by an optimum Gibbs free energy of 2×2 WB_4 nanosheet. Our results, here, not only provide a versatile platform for hosting multiple Dirac semimetal states with a “sandwich” configuration, but also offer a guiding principle for discovering the relationship between intrinsic properties of the active center and the catalytic activity of metal layer from the emerging field of noble-metal-free lattices.

RESULTS AND DISCUSSION

Characterization of WB_4

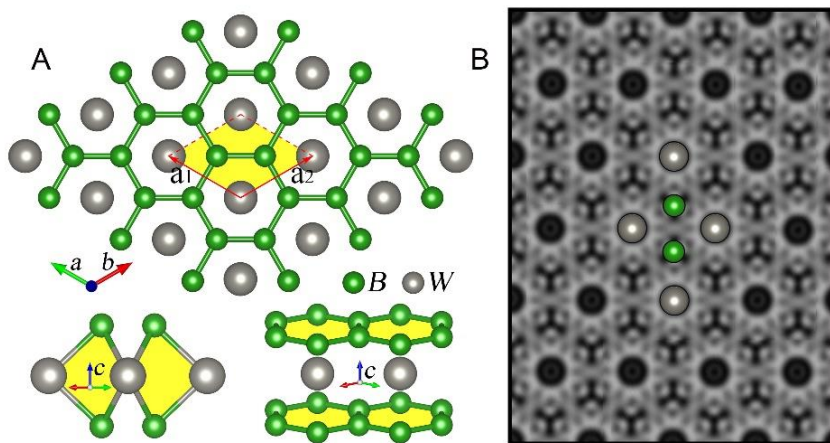


Figure 1. Physical Characterization of WB_4

(A) Schematic representation of the 2D honeycomb tungsten boride (WB_4). The unit cell is indicated by the yellow shaded area with the two basis vectors of \mathbf{a}_1 and \mathbf{a}_2 .

(B) Simulated STM image for monolayer WB_4 .

Experimentally, the WB_2 is found in the hexagonal phase within $P6/mmm$ space group with few freedom of atomic positions [25]. Only on this alone, WB_4 monolayer can be naturally produced through exfoliation of the nanosheet (Supplemental Information). **Figure 1A** represents the top

view and side view, respectively, of the optimized configuration, where the triangle lattice W atoms are located above the center of the honeycomb graphene-like boron lattice from the top view, form a “sandwich”. The lengths are 1.706 Å, 2.371 Å and 2.955 Å for covalent B-B, ionic W-B and metallic W-W bonds, respectively, and the optimized lattice constant is found to be 2.955 Å, matching with the trigonal W lattice in WB₂.

Then, the thermodynamic stability of the WB₄ framework is confirmed by the phonon spectrum calculated along the highly symmetric directions in BZ (**Figure S3**). Clearly, the phonon spectrum of WB₄ lattice is free from imaginary frequencies, implying the thermodynamic stability of WB₄ lattice. By comparing the cleavage energy, it is verified that WB₄ lattice is robust stable than WB₂ in the process of synthetic 2D tungsten boride lattice. So, it can be regarded as WB₄ multilayers, and a single layer of large dimensions is plausible in near future thanks to the well-developed preparative technique (Supplemental Information). To offer more reference information to the experimental observation, the simulated STM image of WB₄ monolayer is also displayed (**Figure 1B**).

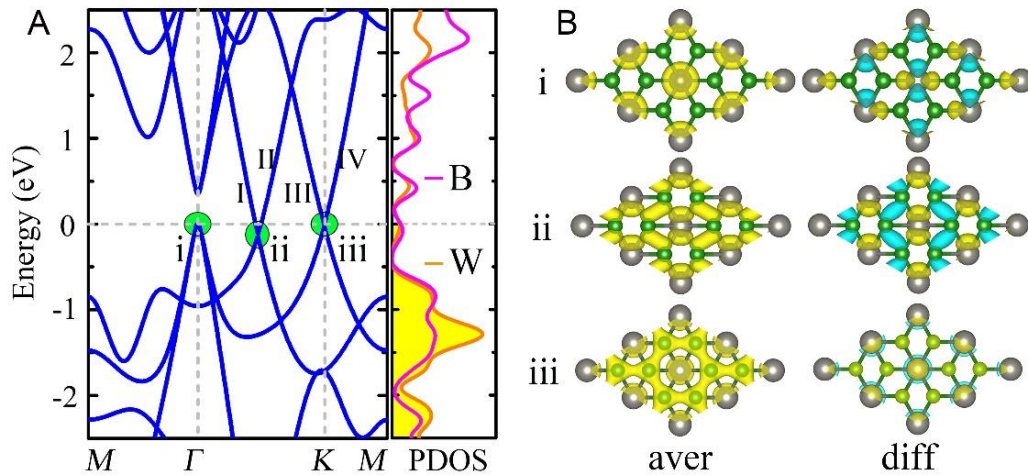


Figure 2. Electrical Characterization of WB₄

(A) Electronic band lines and the corresponding electronic density of states of WB₄ in proximity of the Fermi level (set to zero).

(B) The isosurfaces of the Kohn-Sham wave functions of degenerate points listed in (A). Different colors represent different bands in diff.

Excellent Electrical Transport Property

The electronic properties including the band structure and corresponding projected electronic density of states are presented (**Figure 2A**). Based on density-functional theory (DFT) calculations, two Dirac cones exist closely to the Fermi level (E_f), exhibiting the characteristic of semimetals. By plotting the orbital-resolved band structures as well as the charge density distributions, it is clearly seen that the Dirac bands are composed mainly of the p states of B atoms and the d states of W atoms. More specifically, bands I and II are from the coupling of $p_{x/y/z}$ orbitals of B atoms and the $d_{z^2}/d_{x^2-y^2}/d_{xy}$ orbitals of W atoms, meanwhile, bands III and IV are mainly derived from the coupling of p_z orbital of B and W atoms, together with the d_{xz}/d_{yz} orbitals of W atom (**Figure S4** and **Figure S5**).

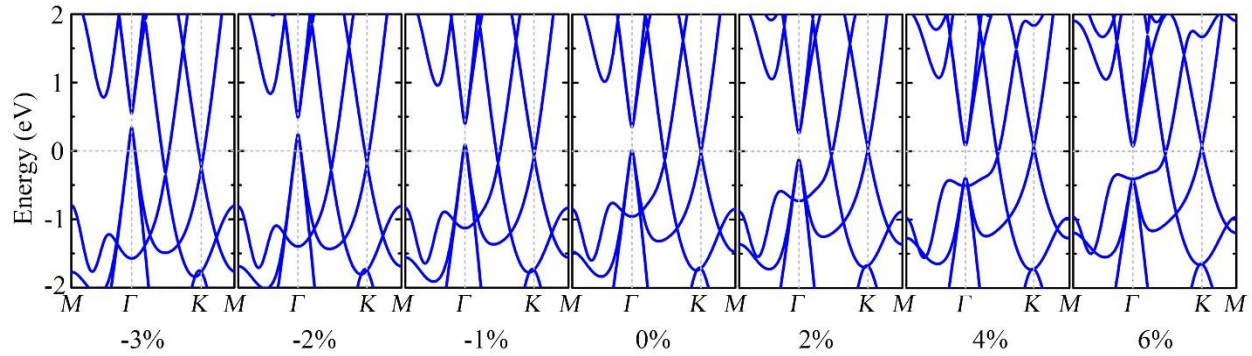


Figure 3. Strain Response of the Semimetal State in WB₄

Electronic band structure evolution of the 2D WB₄ lattice with external strain along the xy -direction. The energy at the Fermi level was set to zero. Here, “-” represents the condition of compressional strain.

Apart from the equalitarian state, we also investigate the robustness of semimetal states under finite biaxial strain. **Figure 3** shows that the semimetal feature is robust against the stretching along the xy -direction, but gradually converts into metal characteristic with abundant states around E_f under the compressional condition, suggesting a different strain response of WB₄. The Fermi velocity (v_f) of the WB₄ lattice was calculated by fitting those Dirac bands and achieved extreme values at the equalitarian state, 0.72×10^6 m/s for band I, 0.54×10^6 m/s for band II and 0.61×10^6 m/s for bands III and IV (Supplemental Information). The multiple Dirac states (different location, origin and anisotropies/isotropies), together with their considerable fermi velocities, should enable

WB₄ monolayer to transfer electrons in all directions throughout its structure, suggesting its excellent electronic transport property.

Hydrogen Evolution Reaction Activity

The metallic property is favorable for the electron injection from a cathode to the catalyst surface, where intermediate protons induced by water dissociation in alkaline solutions are reduced and adsorbed on the catalyst-covered cathode [26]. Hence, we study electrocatalysis applications of the Dirac semimetal lattice with high carrier mobility. Both experimentally and theoretically, the Volmer step is recognized as the rate-determining step for HER [27-29], so, the Gibbs free energy of the adsorption atomic hydrogen (ΔG_H) is the key operator to describe the HER activity [30]. Here, we adopt a (2×2) supercell of WB₄ lattice to study its catalytic activity and find that the bridge site is the most stable adsorption site (**Figure 4A** and Supplemental Information). Therefore, we will only focus on the bridge site hereafter.

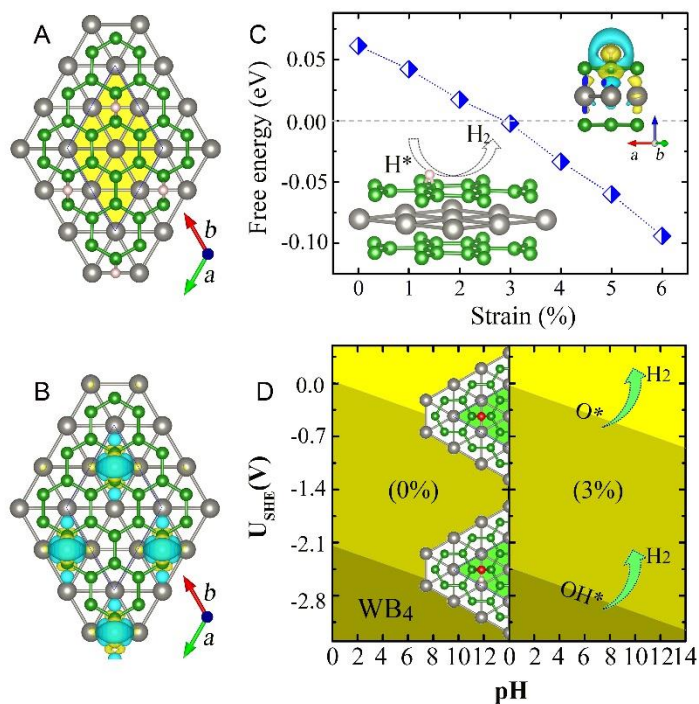


Figure 4. Identification of Active Sites and HER Performance

(A and B) Schematic representation of (2×2) WB₄ 2D supercell with a hydrogen adsorption (A) and the corresponding charge density difference before and after the adsorption (B). The unit cell is indicated by the yellow shaded area.

(C) Gibbs free energy diagram of HER in strained states. Blue and yellow represent charge loss and charge accumulation, respectively. The isosurface value is set to 0.002\AA^{-3} .

(D) Surface pourbaix diagrams. The most thermodynamically stable states of the surface under relevant U_{SHE} conditions and pH values are labeled by the terminations. The optimized structures of hydroxyl-terminated WB_4 and oxygen-terminated WB_4 were listed in the insert figure. Oxygen is represented by the red ball.

In order to elucidate the adsorption mechanism, we further analyze the charge transfer between with and without the hydrogen adsorption, which is defined as $\Delta Q = Q(\text{sub}+\text{H}) - Q(\text{sub}) - Q(\text{H})$, where $Q(\text{sub}+\text{H})$, $Q(\text{sub})$ and $Q(\text{H})$ are the charge densities of the corresponding WB_4 systems with a hydrogen adsorption, the clean corresponding WB_4 systems and a single hydrogen atom, respectively. As **Figure 4B** shown, charges can transfer between B and H atoms as well as the nearest W atoms, providing a possible platform for catalytic reactions. Formally, the charges are mainly contributed by p -orbitals of B and d -orbitals of W (**Figure S7** and **Figure S8**). Quantitatively, the Bader charge analysis reveals that the hydrogen has a net gain of $2.32e$ from the surrounding B and W atoms, exhibiting an excellent potential performance for HER activity.

Based on the PBE functional, we obtained the Gibbs free energy $\Delta G_{\text{H}} = 0.06$ eV for the above WB_4 nanosheet, indicating that the surface bridge site is catalytically active for HER. Inspired by the experimental stress effect on catalytic activity [31, 32], we investigated the biaxial strain effect on the HER catalytic activity of WB_4 lattice, and the related Gibbs free energies are calculated (**Figure 4C**). Interestingly, the ΔG_{H} of WB_4 nanosheet responds differently to the above-mentioned Dirac semimetal states. For example, the stretch makes the WB_4 nanosheet approaching the ideal catalytic state ($\Delta G_{\text{H}} \sim 0.00$ eV) firstly, and then far away the state with further increased stretch, suggesting that WB_4 nanosheet has a good HER performance within a certain tensile strain.

Controlled d band Mechanisms

To analyze the origin of the catalytic activity evolution, we examined how the d -band center can be modulate with the change of strain in WB_4 nanosheet. Considering the orbital hybridization between W and W atoms (the distance ranges from 2.955\AA to 3.132\AA), the d -orbitals of four W atoms are plotting (**Figure 5**) and their d -band centers are marked by black arrows. According to

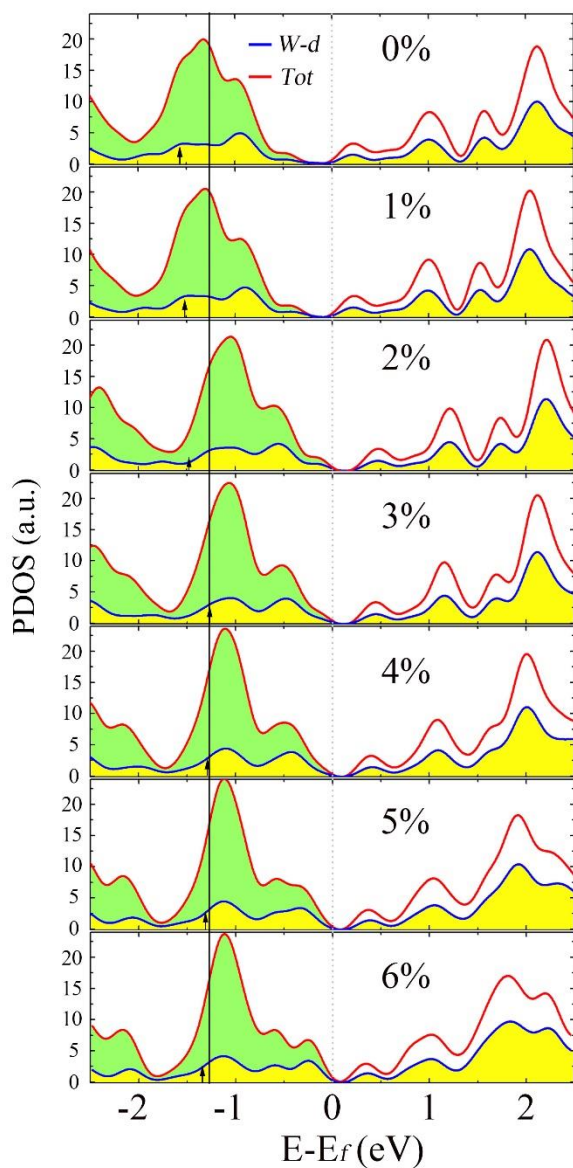


Figure 5. Evolution of d Band Center

The projected density of states for the d -orbitals of W in the strained states. The vertical black lines correspond to the location of strained states with 3% which has the highest catalytic activity. The energy at the Fermi level was set to zero.

the d -band theory, a lower d -band center results in weaker bonding between the catalyst and the adsorbate [33]. Taking the zero-point energy (ZPE) and entropy into account, the relative catalytic activity of WB_4 (ΔG_H) has similar evolutionary relationship with the d band center (**Figure 4C**, **Figure 5** and **Figure S12**). The results can be attributed to the existence of B intermediate, which are modulating the combination of W with H to make a mild catalytic reaction by changing the coupling interactions between d -orbitals of W and p -orbitals of B. The coupling interactions makes the d -orbitals center of W shifting to a more negative value, resulting in a better catalytic activity. Additionally, the desorption barrier ($\Delta G_H \sim -0.06$ eV) of 5% strained state equals the adsorption

barrier ($\Delta G_H \sim 0.06$ eV) of 0% equalitarian state, so we can get the maximum adsorption and desorption by manipulating a small external stress to get an ideal catalytic state.

Except the modulated d -band center, the excellent conductivity and Fermi velocity, induced by the effect of Dirac cone with d - p - π and d - p - σ conjugations, also can guarantee fast electron transfer on the process of electrochemical reactions. Therefore, our results not only provide a guiding principle for the discovery of Dirac semimetal catalyst with noble-metal-free “sandwich” configuration, but also offer a universal description of the relationship between intrinsic properties of the active center and the catalytic activity of metal layer, which are in line with new research frontier in single-atom electrocatalysts [34-36].

High Thermal Stability

The surface Pourbaix diagrams of the equalitarian (0%) and strained (3%) states are constructed by plotting the thermodynamically most stable surface state under the relevant U_{SHE} and pH values (**Figure 4D**). In an acidic solution (pH = 0), negative U_{SHE} values (reducing environment) as low as -2.14 and -2.43 V are required to protect the equalitarian state and strained state, respectively, from oxidation by H_2O . A more negative potential is necessary to protect the bare WB_4 lattice at high pH values with a slope of -0.059 V/pH. When the potential is above the cathodic protection potential of the 2D WB_4 , water starts to oxidize and the WB_4 is covered by one hydroxyl (OH^*). As the potential increases, the hydroxyls on WB_4 will be oxidized, and the most stable O^* -terminated WB_4 will be formed. The lowest U_{SHE} values for 2D WB_4 with one O^* termination are 0.03 V (0%) and -0.03 (3%) in an acidic solution. Therefore, under standard conditions, the strained state prefers to be terminated by O^* , exhibits a better HER performance fitting with ΔG_H descriptor (Supplemental Information).

Hydrogen Coverage Effect in WB_4

Finally, we explore the hydrogen coverage effect on the HER catalytic performance of the 0% and 3% states. We define the coverage of hydrogen as the fraction of a monolayer with respect to the number of available B-B bridge sites (12 sites) in the basal plane. Here, we consider one ($\sigma = 1/12$), two ($\sigma = 1/6$), three ($\sigma = 1/4$) and four ($\sigma = 1/3$) hydrogen adsorption in 2×2 WB_4 supercell and calculate Gibbs free energies as summarized in **Figure 6** and Supplemental Information. As a benchmark, we firstly calculate the HER performance of Pt with $\Delta G_H = -0.05$ eV, fitting well with

other previous works [30, 34]. Interestingly, the variation of the Gibbs free energy is obvious with the increase of H coverage, indicating that ΔG_H is sensitive to the hydrogen coverage. Typically, the 3% strained state at $\sigma = 1/3$ has a free energy of 0.02 eV, whose catalytic performance even exceeds that of Pt. Hence, considering the Pt-like activity for HER of WB₄, a series of the 2D noble-metal-free “sandwich” lattices should be promising materials to replace Pt or Pt compound in other electrochemical and photoelectrochemical applications.

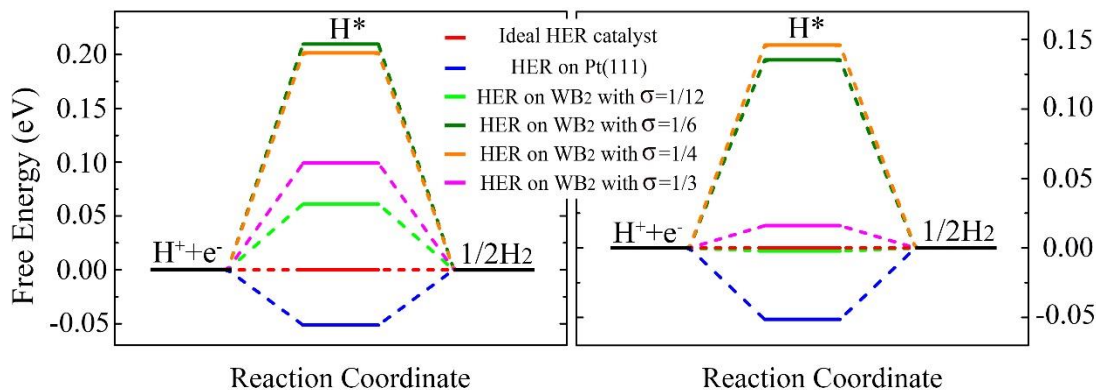


Figure 6. Evolution of ΔG_H in Different Coverages

Gibbs free energy diagram of HER under different coverage at equilibrium potential. As a benchmark, the Gibbs free energy for Pt was calculated by the same strategy and listed here.

EXPERIMENTAL PROCEDURES

Computational Details of DFT Calculations

The first-principles calculations within density-functional theory (DFT) were implemented by the Vienna *ab-initio* Simulation Package (VASP) [37]. A generalized gradient approximation (GGA) in the form of Perdew-Burke-Ernzerhof (PBE) [38] was adopted to describe the electron-electron interactions. The energy cut-off employed for plane-wave expansion of electron wavefunctions was set to 520 eV and the electron-ion interactions were treated using projector-augmented-wave (PAW) potentials [39]. The DFT-D3 method was applied to include the long-range van der Waals interaction for the adsorption on WB₄ lattice [40]. The system was modeled by unit cells repeated periodically on the x - y plane, while a vacuum region of 15 Å was applied along the z -direction to avoid mirror interaction between neighboring images. The Brillouin zone (BZ) integration was sampled on a grid of $13 \times 13 \times 1$ k -points for the unit cell and $7 \times 7 \times 1$ k -points for the $2 \times 2 \times 1$ supercell.

Structure optimization was carried out using a conjugate gradient (CG) method until the remaining force on each atom is less than 0.05 eV/Å.

Gibbs Free Energy of Hydrogen Adsorption

The adsorption Gibbs free-energy of hydrogen, ΔG_H , is a good descriptor for hydrogen evolution [41, 42], which is defined as $\Delta G_H = \Delta E_H + \Delta E_{ZPE} - T\Delta S_H$. ΔE_H is the hydrogen adsorption energy, which can be obtained as following: $\Delta E_H = E_{nH^*} - E_{(n-1)H^*} - 1/2 E_{H_2}$, where * donates the catalyst activity site. E_{nH^*} , $E_{(n-1)H^*}$ and E_{H_2} are total energies of catalyst with n adsorbed hydrogen atoms, total energies of catalyst with $n-1$ adsorbed hydrogen atoms and gas H_2 , respectively. ΔE_{ZPE} and ΔS_H stand for the change in the ZPE and the change in the entropy of hydrogen between the adsorbed state and the gas state. We found that ΔE_{ZPE} does not vary significantly with respect to hydrogen coverage because of the smaller entropy of hydrogen in the adsorbed state. $T\Delta S_H \approx TS_H^0 = -0.202$ eV at $T = 298$ K, where S_H^0 is the entropy in the gas phase [43]. The standard hydrogen electrode (U_{SHE}) was theoretically defined in solution [pH = 0, p(H_2) = 1 bar]. The optimal HER activity can be achieved as ΔG_H goes to zero, where both hydrogen adsorption and the subsequent desorption can be facilitated.

ACKNOWLEDGMENTS

M.W.Z. thanks the support from the National Natural Science Foundation of China (Nos. 21433006 and 11774201). Y. P. Feng acknowledges funding support from the A*STAR's Pharos Programme on Topological Insulators (Grant No. 1527400026). The computational resources were provided by the Centre for Advanced 2D Materials of the National University of Singapore in Singapore and the National Super Computing Centre in Jinan.

DECLARATION OF INTERESTS

The authors declare no competing interests.

REFERENCES

[1] Esposito, D.V., Hunt, S.T., Stottlemeyer, A.L., Dobson, K.D., McCandless, B.E., Birkmire, R.W., and Chen, J.G. (2010). Low-Cost Hydrogen-Evolution Catalysts Based on Monolayer Platinum on Tungsten Monocarbide Substrates. *Angew. Chem. Int. Ed.* 49, 9859-9862.

- [2] Jang, S.-E., and Kim, H. (2010). Effect of water electrolysis catalysts on carbon corrosion in polymer electrolyte membrane fuel cells. *J. Am. Chem. Soc.*, 132, 14700-14701.
- [3] Wang, Y.-J., Zhao, N., Fang, B., Li, H., Bi, X.T., and Wang, H. (2015). Carbon-supported Pt-based alloy electrocatalysts for the oxygen reduction reaction in polymer electrolyte membrane fuel cells: particle size, shape, and composition manipulation and their impact to activity. *Chem. Rev.*, 115, 3433-3467.
- [4] Wu, X., and Scott, K. (2011). RuO₂ supported on Sb-doped SnO₂ nanoparticles for polymer electrolyte membrane water electrolyzers. *Int. J. Hydrogen Energy*, 36, 5806-5810.
- [5] Li, Y., Takata, T., Cha, D., Takanabe, K., Minegishi, T., Kubota, J., and Domen, K. (2013). Vertically Aligned Ta₃N₅ Nanorod Arrays for Solar-Driven Photoelectrochemical Water Splitting. *Adv. Mater.*, 25, 125-131.
- [6] Ager, J.W., Shaner, M.R., Walczak, K.A., Sharp, I.D., and Ardo, S. (2015). Experimental demonstrations of spontaneous, solar-driven photoelectrochemical water splitting. *Energy Environ. Sci.*, 8, 2811-2824.
- [7] Youngblood, W.J., Lee, S.-H.A., Kobayashi, Y., Hernandez-Pagan, E.A., Hoertz, P.G., Moore, T.A., Moore, A.L., Gust, D., and Mallouk, T.E. (2009). Photoassisted overall water splitting in a visible light-absorbing dye-sensitized photoelectrochemical cell. *J. Am. Chem. Soc.*, 131, 926-927.
- [8] Yang, C.-J. (2009). An impending platinum crisis and its implications for the future of the automobile. *Energy Policy*, 37, 1805-1808.
- [9] Subbaraman, R., Tripkovic, D., Strmcnik, D., Chang, K.C., Uchimura, M., Paulikas, A.P., Stamenkovic, V., and Markovic, N.M. (2011). Enhancing hydrogen evolution activity in water splitting by tailoring Li(+)-Ni(OH)₂-Pt interfaces. *Science*, 334, 1256-1260.
- [10] Wang, P., Jiang, K., Wang, G., Yao, J., and Huang, X. (2016). Phase and Interface Engineering of Platinum-Nickel Nanowires for Efficient Electrochemical Hydrogen Evolution. *Angew. Chem.*, 55, 12859-12863.
- [11] Wang, P., Zhang, X., Zhang, J., Wan, S., Guo, S., Lu, G., Yao, J., and Huang, X. (2017). Precise tuning in platinum-nickel/nickel sulfide interface nanowires for synergistic hydrogen evolution catalysis. *Nat. Commun.*, 8, 14580.
- [12] Seh, Z.W., Kibsgaard, J., Dickens, C.F., Chorkendorff, I., Norskov, J.K., and Jaramillo, T.F. (2017). Combining theory and experiment in electrocatalysis: Insights into materials design. *Science*, 355, eaad4998.

- [13] Feng, J.X., Wu, J.Q., Tong, Y.X., and Li, G.R. (2018). Efficient Hydrogen Evolution on Cu Nanodots-Decorated Ni₃S₂ Nanotubes by Optimizing Atomic Hydrogen Adsorption and Desorption. *J. Am. Chem. Soc.*, 140, 610-617.
- [14] Feng, J.X., Tong, S.Y., Tong, Y.X., and Li, G.R. (2018). Pt-like Hydrogen Evolution Electrocatalysis on PANI/CoP Hybrid Nanowires by Weakening the Shackles of Hydrogen Ions on the Surfaces of Catalysts. *J. Am. Chem. Soc.*, 140, 5118-5126.
- [15] Zhang, X., Luo, Z., Yu, P., Cai, Y., Du, Y., Wu, D., Gao, S., Tan, C., Li, Z., Ren, M., et al. (2018). Lithiation-induced amorphization of Pd₃P₂S₈ for highly efficient hydrogen evolution. *Nat. Catal.*, 1, 460-468.
- [16] Nong, S., Dong, W., Yin, J., Dong, B., Lu, Y., Yuan, X., Wang, X., Bu, K., Chen, M., Jiang, S., Liu, L., Sui, M., Huang, F., (2018) Well-Dispersed Ruthenium in Mesoporous Crystal TiO₂ as an Advanced Electrocatalyst for Hydrogen Evolution Reaction. *J. Am. Chem. Soc.*, 140, 5719-5727.
- [17] Oganov, A.R., Chen, J., Gatti, C., Ma, Y., Ma, Y., Glass, C.W., Liu, Z., Yu, T., Kurakevych, O.O., and Solozhenko, V.L. (2009). Ionic high-pressure form of elemental boron. *Nature*, 457, 863.
- [18] Huang, W., Sergeeva, A.P., Zhai, H.-J., Averkiev, B.B., Wang, L.-S., and Boldyrev, A.I. (2010). A concentric planar doubly π -aromatic B₁₉-cluster. *Nat. Chem.*, 2, 202.
- [19] Bezugly, V., Kunstmann, J., Grundkötter-Stock, B., Frauenheim, T., Niehaus, T., and Cuniberti, G. (2011). Highly conductive boron nanotubes: transport properties, work functions, and structural stabilities. *ACS Nano*, 5, 4997-5005.
- [20] Zhang, Z., Penev, E.S., and Yakobson, B.I. (2016). Two-dimensional materials: polyphony in B flat. *Nat. Chem.*, 8, 525.
- [21] Decker, B., and Kasper, J. (1959). The crystal structure of a simple rhombohedral form of boron. *Acta Crystallogr.*, 12, 503-506.
- [22] Chen, Y., Yu, G., Chen, W., Liu, Y., Li, G.D., Zhu, P., Tao, Q., Li, Q., Liu, J., Shen, X., et al. (2017). Highly Active, Nonprecious Electrocatalyst Comprising Borophene Subunits for the Hydrogen Evolution Reaction. *J. Am. Chem. Soc.*, 139, 12370-12373.
- [23] Park, H., Encinas, A., Scheifers, J.P., Zhang, Y., and Fokwa, B.P.T. (2017). Boron-Dependency of Molybdenum Boride Electrocatalysts for the Hydrogen Evolution Reaction. *Angew. Chem.*, 56, 5575-5578.

- [24] Li, Q., Zou, X., Ai, X., Chen, H., Sun, L., and Zou, X. (2018). Revealing Activity Trends of Metal Diborides Toward pH-Universal Hydrogen Evolution Electrocatalysts with Pt-Like Activity. *Adv. Energy Mater.*, 1803369.
- [25] Woods, H., Wawner, F., and Fox, B.G. (1966). Tungsten diboride: preparation and structure. *Science*, 151, 75-75.
- [26] Zou, X., and Zhang, Y. (2015). Noble metal-free hydrogen evolution catalysts for water splitting. *Chem. Soc. Rev.*, 44, 5148-5180.
- [27] Gao, M.-R., Liang, J.-X., Zheng, Y.-R., Xu, Y.-F., Jiang, J., Gao, Q., Li, J., and Yu, S.-H. (2015). An efficient molybdenum disulfide/cobalt diselenide hybrid catalyst for electrochemical hydrogen generation. *Nat. Commun.*, 6, 5982.
- [28] Gao, G., O'Mullane, A.P., and Du, A. (2016). 2D MXenes: A new family of promising catalysts for the hydrogen evolution reaction. *ACS Catal.*, 7, 494-500.
- [29] Gao, G., Jiao, Y., Ma, F., Jiao, Y., Waclawik, E., and Du, A. (2015). Metal-free graphitic carbon nitride as mechano-catalyst for hydrogen evolution reaction. *J. Catal.*, 332, 149-155.
- [30] Nørskov, J.K., Bligaard, T., Logadottir, A., Kitchin, J., Chen, J.G., Pandelov, S., and Stimming, U. (2005). Trends in the exchange current for hydrogen evolution. *J. Electrochem. Soc.*, 152, J23-J26.
- [31] Voiry, D., Yamaguchi, H., Li, J., Silva, R., Alves, D.C., Fujita, T., Chen, M., Asefa, T., Shenoy, V.B., and Eda, G. (2013). Enhanced catalytic activity in strained chemically exfoliated WS₂ nanosheets for hydrogen evolution. *Nat. Mater.*, 12, 850.
- [32] Li, H., Tsai, C., Koh, A.L., Cai, L., Contryman, A.W., Fragapane, A.H., Zhao, J., Han, H.S., Manoharan, H.C., and Abild-Pedersen, F. (2016). Activating and optimizing MoS₂ basal planes for hydrogen evolution through the formation of strained sulphur vacancies. *Nat. Mater.*, 15, 48.
- [33] Gong, Q., Wang, Y., Hu, Q., Zhou, J., Feng, R., Duchesne, P.N., Zhang, P., Chen, F., Han, N., and Li, Y. (2016). Ultrasmall and phase-pure W₂C nanoparticles for efficient electrocatalytic and photoelectrochemical hydrogen evolution. *Nat. Commun.*, 7, 13216.
- [34] Xu, H., Cheng, D., Cao, D., and Zeng, X.C. (2018). A universal principle for a rational design of single-atom electrocatalysts. *Nat. Catal.*, 1, 339-348.
- [35] Yang, X.-F., Wang, A., Qiao, B., Li, J., Liu, J., and Zhang, T. (2013). Single-atom catalysts: a new frontier in heterogeneous catalysis. *Accounts Chem. Res.*, 46, 1740-1748.

- [36] Qiao, B., Wang, A., Yang, X., Allard, L.F., Jiang, Z., Cui, Y., Liu, J., Li, J., and Zhang, T. (2011). Single-atom catalysis of CO oxidation using Pt₁/FeO_x. *Nat. Chem.*, 3, 634.
- [37] Kresse, G., and Hafner, J. (1994). Norm-conserving and ultrasoft pseudopotentials for first-row and transition elements. *J. Phys.: Condens. Mat.*, 6, 8245.
- [38] Perdew, J.P., Burke, K., and Ernzerhof, M. (1996). Generalized gradient approximation made simple. *Phys. Rev. Lett.*, 77, 3865.
- [39] Kresse, G., and Joubert, D. (1999). From ultrasoft pseudopotentials to the projector augmented-wave method. *Phys. Rev. B*, 59, 1758.
- [40] Grimme, S., Ehrlich, S., and Goerigk, L. (2011). Effect of the damping function in dispersion corrected density functional theory. *J. Comput. Chem.*, 32, 1456-1465.
- [41] Conway, B., and Bockris, J.O.M. (1957). Electrolytic hydrogen evolution kinetics and its relation to the electronic and adsorptive properties of the metal. *J. Chem. Phys.*, 26, 532-541.
- [42] Parsons, R. (1958). The rate of electrolytic hydrogen evolution and the heat of adsorption of hydrogen. *Trans. Faraday. Soc.*, 54, 1053-1063.
- [43] Atkins, P., and De Paula, J. (2013). *Elements of physical chemistry* (Oxford University Press, USA), 10th ed, pp: 1-1008.

Supporting Information for

Tungsten Boride: a 2D Multiple Dirac Semimetal for Hydrogen Evolution Reaction

Aizhu Wang^{1,2}, Lei Shen³, Mingwen Zhao^{4*}, Junru Wang⁴, Weifeng Li⁴, Weijia Zhou¹,
Yuanping Feng^{5*}, and Hong Liu^{1,6*}

¹*Institute for Advanced Interdisciplinary Research, University of Jinan, Jinan, Shandong, 250022, China*

²*Department of Electrical and Computer Engineering and Department of Physics, National University of Singapore, Singapore, 117579, Singapore*

³*Department of Mechanical Engineering, Engineering Science Programme, Faculty of Engineering, National University of Singapore, Singapore, 117575, Singapore*

⁴*School of Physics and State Key Laboratory of Crystal Materials, Shandong University, Jinan 250100, Shandong, China*

⁵*Department of Physics & Centre for Advanced Two-dimensional Materials, National University of Singapore, Singapore, 117542, Singapore*

⁶*State Key Laboratory of Crystal Materials, Shandong University, Jinan, 250100, Shandong, China*

*Correspondences:

zmw@sdu.edu.cn (M. Z.)

phyfyp@nus.edu.sg (Y. F.)

hongliu@sdu.edu.cn (H. L.)

Part I The band structures of tungsten diboride

Figure S1(a) gives the top view and side view, respectively, of the tungsten diboride configuration, where the triangle lattice W atoms are located above the center of the honeycomb graphene-like boron lattice from the top view, form a “sandwich”. The bond lengths are 1.746 Å, 2.513 Å and 3.025 Å for B-B, W-B and W-W, respectively. Values of $a = 3.025$ and $c = 3.329$ is calculated for a hexagonal unit cell, fitting well with the experiment data ($a = 3.020$ and $c = 3.050$). Clearly, the bulk materials are metallic with several bands across the Fermi level, as shown in the electronic band structure (Figure S1(b)). This is in good agreement with good electron conductivity of the tungsten diboride found in experiments [1].

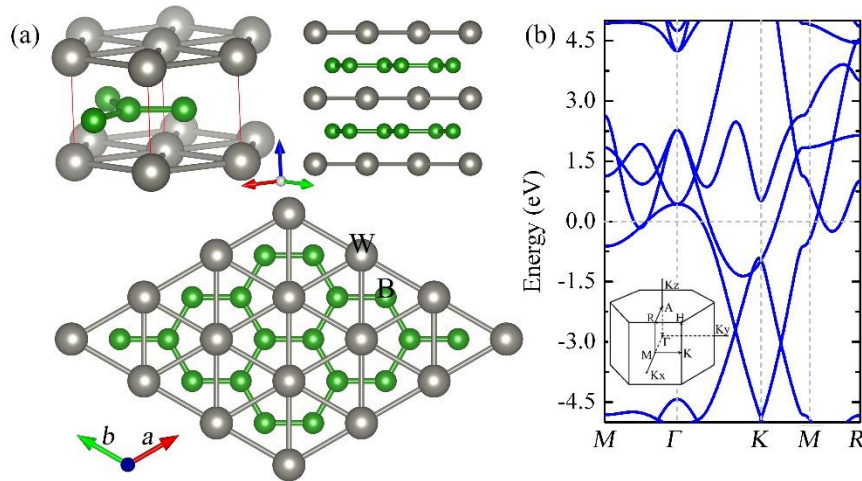


Figure S1 (a) Schematic illustration of fabrication of WB_2 (P6/mmm, number 191) crystal. The unit cell is indicated by the red line. (b) The calculated band structures based on PBE calculations were also listed here. The energy at the Fermi level was set to zero.

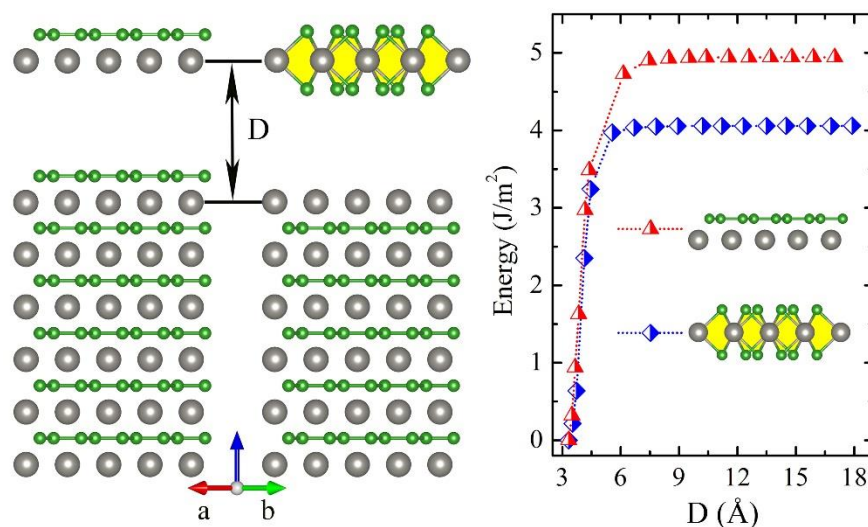


Figure S2 (a) Schematic representation of the exfoliation process of WB₂ monolayer and WB₄ monolayer. (b) Energy increase E as a function of interlayer distance (D).

Then, the possibility of producing WB₄ monolayer using a mechanical exfoliation strategy was confirmed (Figure 2S). The cleavage energy E_{cl} is defined as the minimum energy required to exfoliate a monolayer from bulk. We used a seven-slab model to mimic a bulk material and calculated the energy increase as a WB₄ monolayer is exfoliated from the slab. A vacuum layer at least 15 Å was incorporated into the seven-layer slab to avoid the artificial interaction between two neighboring slabs. Figure S2 gives the variation of energy (and its derivative) as a function of the interlayer distance (D) between the top most monolayer and the remnant layers, which was fixed during the exfoliation process. The calculated cleavage energy E_{cl} of WB₄ is about 4.06 J m⁻². The cleavage strength (χ) was further obtained from the derivative of energy with respect to the distance, which is about 2.66 GPa. It is noteworthy that the calculated cleavage energy of WB₄ is smaller than that of WB₂ suggesting high plausibility to extract the WB₄ monolayer from the bulk in experiments.

Part II The thermodynamic stability and electrical properties of WB₄

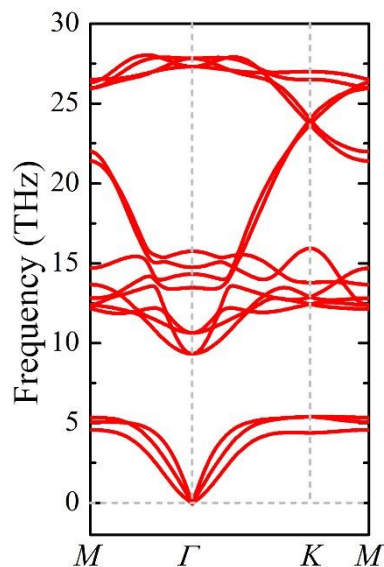


Figure S3 (Color online) Phonon spectrum of WB₄ along the high symmetric points in BZ.

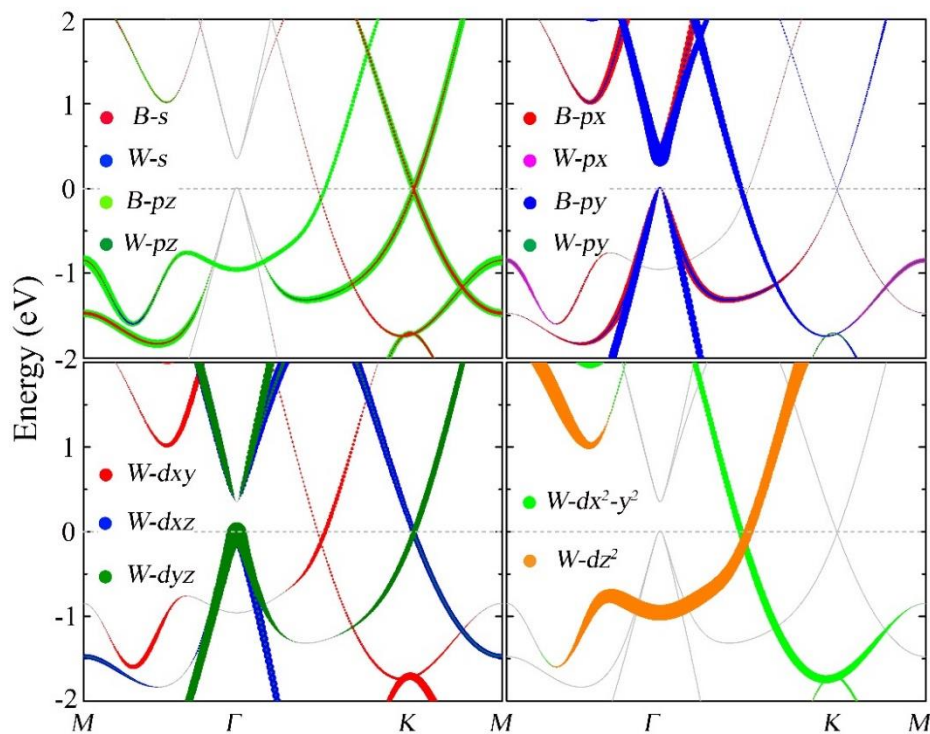


Figure S4. (Color online) Orbital-resolved band structures around Fermi level based on PBE calculations. The size of colorful dots is proportion to the contribution of the different orbitals on the wave function. The energy at the Fermi level was set to zero.

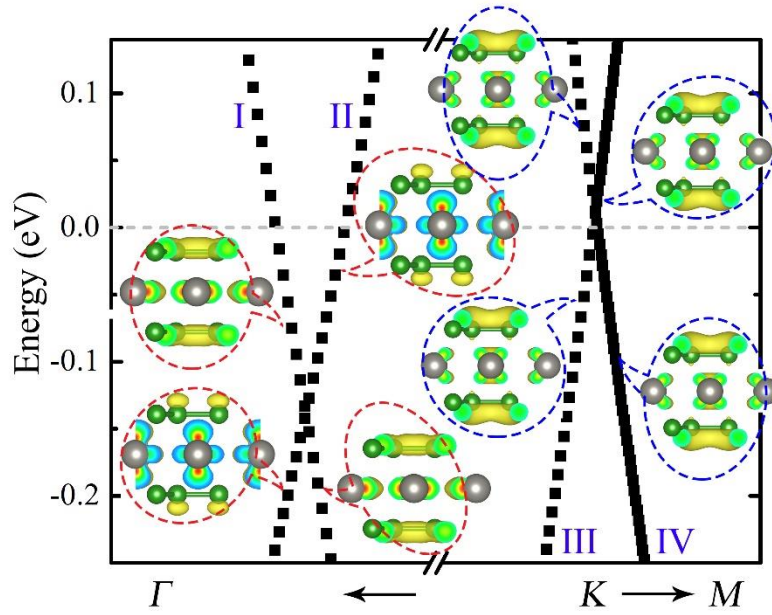


Figure S5. Charge density distributions near the Fermi level, both Dirac cone (cone ii and cone iii) are from d orbitals of W and p orbitals of B atoms. Cone iii, made up of bands III and IV, is isotropic with a high symmetry, while, cone ii, made up of bands I and II, is anisotropic with a lower symmetry. The energy at the Fermi level was set to zero.

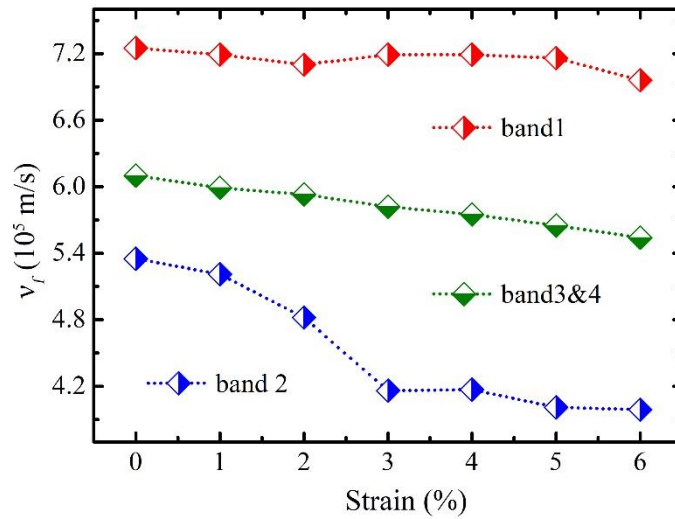


Figure S6 Fermi velocity evolutions of Dirac bands in the 2D WB_4 lattice with external stretching strain along the xy -direction.

The charge carriers in these linear bands will behave as massless Dirac fermions. The Fermi velocity (v_f) of the WB₄ lattice can be tested by fitting those Dirac bands at $k = K + q$ to the expression of $v_f = E(q)/\hbar|q|$. The Fermi velocities are 0.72×10^6 m/s (band I), 0.54×10^6 m/s (band II) and 0.61×10^6 m/s (bands III and IV), respectively. These values are approximately 83.72%, 62.72% and 70.85% of that of graphene (0.86×10^6 m/s) from the present calculations. Apart from the equalitarian state, we also investigated the robustness of semimetal states and Fermi velocities of the WB₄ monolayer under finite biaxial strain (-3% ~ 6%). Interestingly, the electronic structure of the WB₄ lattice responds differently to compressive (negative sign) and tensile (positive sign) strains as shown in **Figure 3**. The semimetal feature is robust against the stretching along the xy -direction, but gradually converts into metal characteristic with abundant states around E_f under the compressional condition. As for those semimetal states, thanks for the configure symmetry and the out-of-plane coupling of orbitals (p_z and d_{xz}/d_{yz}), the Dirac cone iii remains intact, but with a linear decreasing v_f from 0.61×10^6 m/s to 0.55×10^6 m/s. Affected by Γ point, the v_f of band I almost keeps a constant, however, the value of band II has a sharp drop as shown in **Figure S6**.

Part III The hydrogen evolution reaction calculations

Here, we adopt a (2×2) WB₄ 2D supercell to study its HER performance. On the basal plane of WB₄, there are three potential hydrogen adsorption sites, *i.e.*, W top site, B top site and the bridge site of B-B bond. The hydrogen adsorption energies on these sites are calculated and summarized in Table 1. The bridge site of B-B bond is the most stable adsorption site with $\Delta E_H = -0.34$ eV. The adsorption of hydrogen is much weak for the B top site (-0.17 eV) and is unfavorable for the W top sites (positive values). Therefore, we will only focus on bridge site hereafter.

Table S1. Hydrogen adsorption energies on potential adsorption sites of WB₄ and the height of the hydrogen atom above the surface.

Adsorption site		Adsorption energy (eV)	Δz (Å)
W top sites	1	5.56	0.27
	2	1.51	0.67
	3	1.51	0.65
B top site		-0.11	1.28
Bridge site of B-B bond		-0.31	1.01

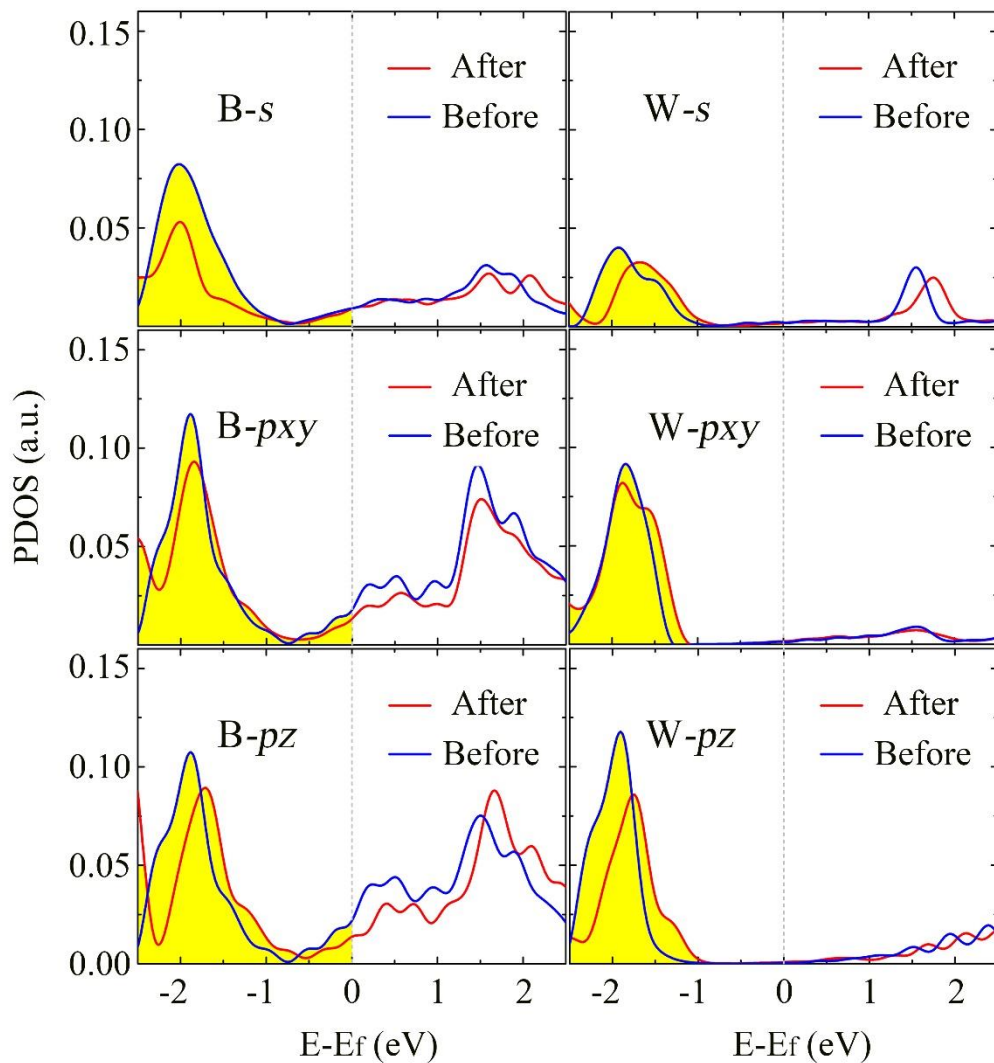


Figure S7 (Color online) The projected density of states (PDOS) for the s - and p -orbitals of B and W atom under the condition with (after) and without (before) hydrogen adsorption. The energy at the Fermi level was set to zero.

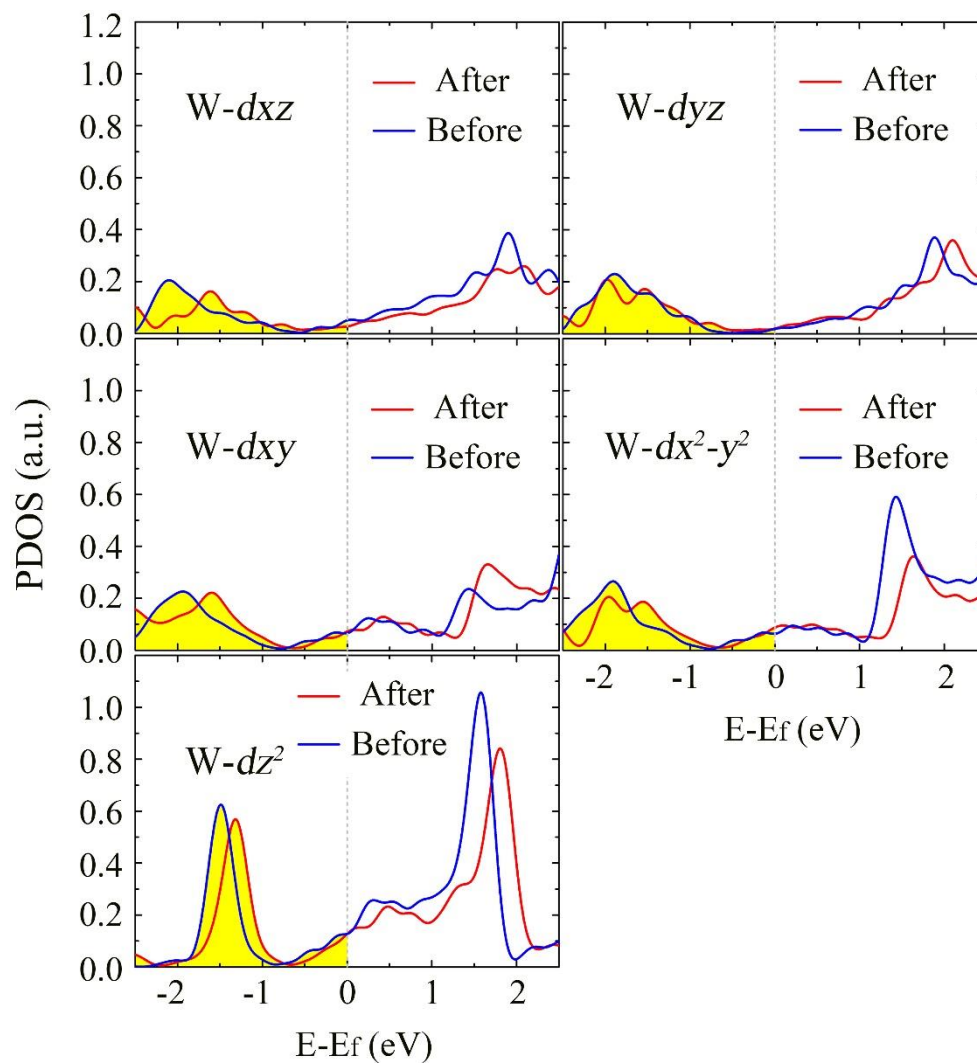


Figure S8 (Color online) The projected density of states (PDOS) for the d -orbitals of W atom under the condition with (after) and without (before) hydrogen adsorption. The energy at the Fermi level was set to zero.

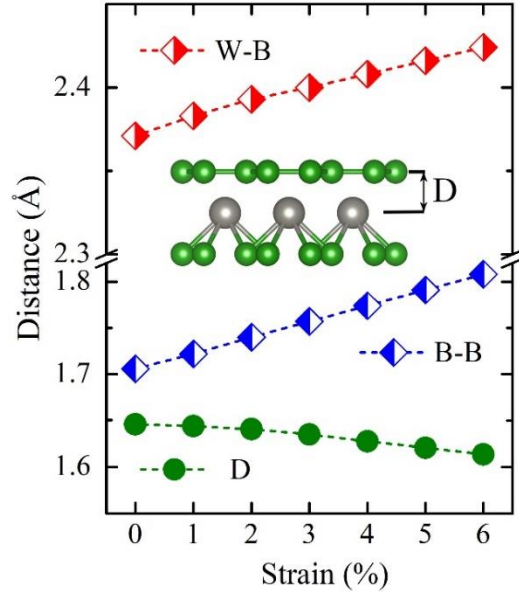


Figure S9 (Color online) The evolutions of bonds. It can be clearly seen that the perpendicular distance between B and W decreases with the increase of lattice constant. And the hybridization between p -orbitals of B atoms and d -orbitals of W will change accordingly.

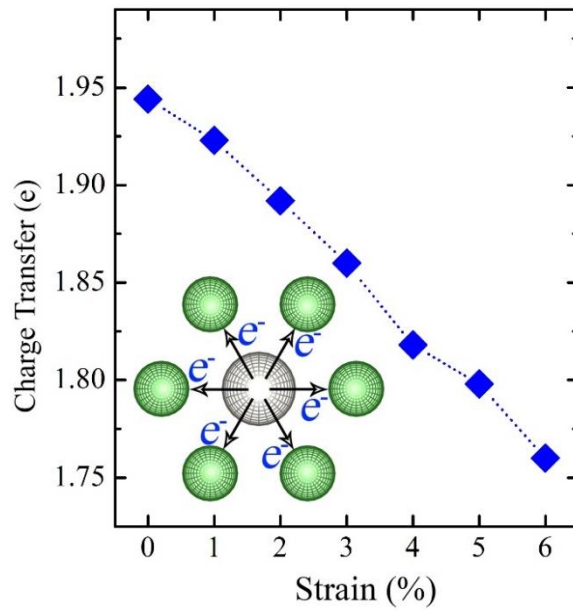


Figure S10 (Color online) The evolutions of charge transfer from W atom to the surrounding B atoms in WB_4 nanosheet without hydrogen adsorption.

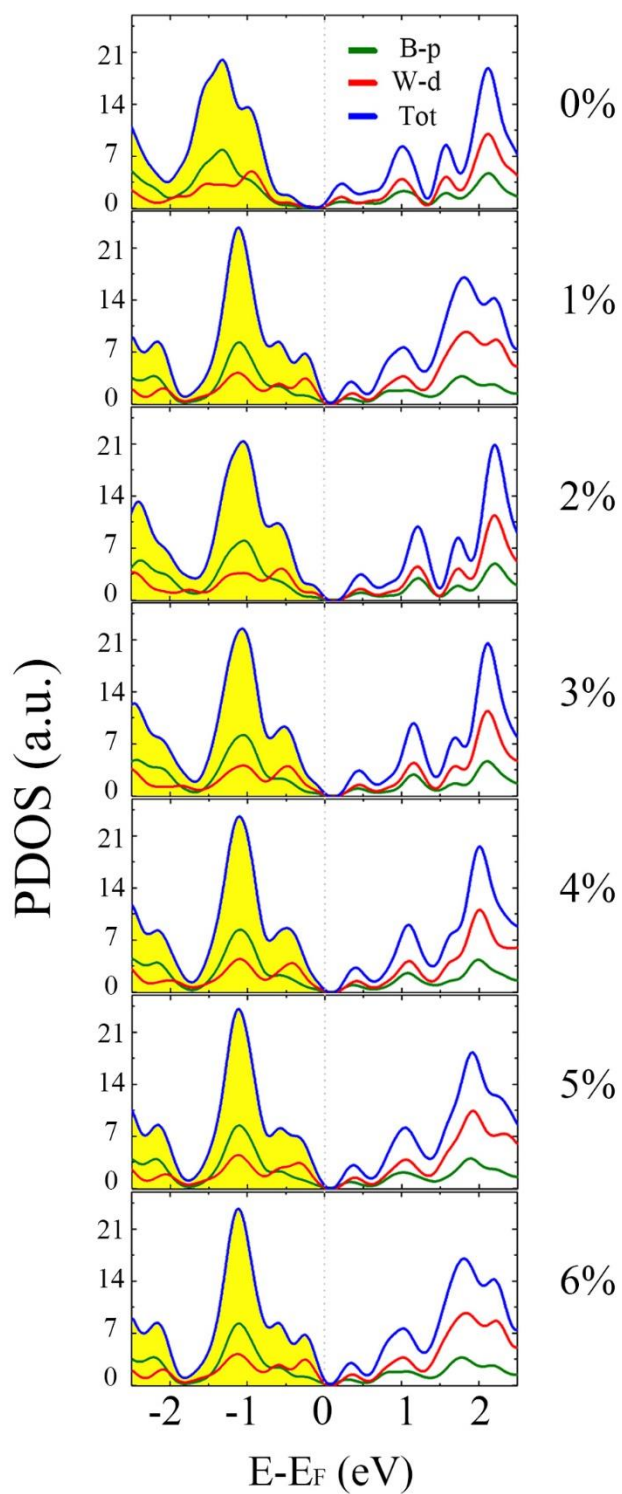


Figure S11 (Color online) The evolutions of the projected density of states (PDOS) for B and W atoms. The energy at the Fermi level was set to zero.

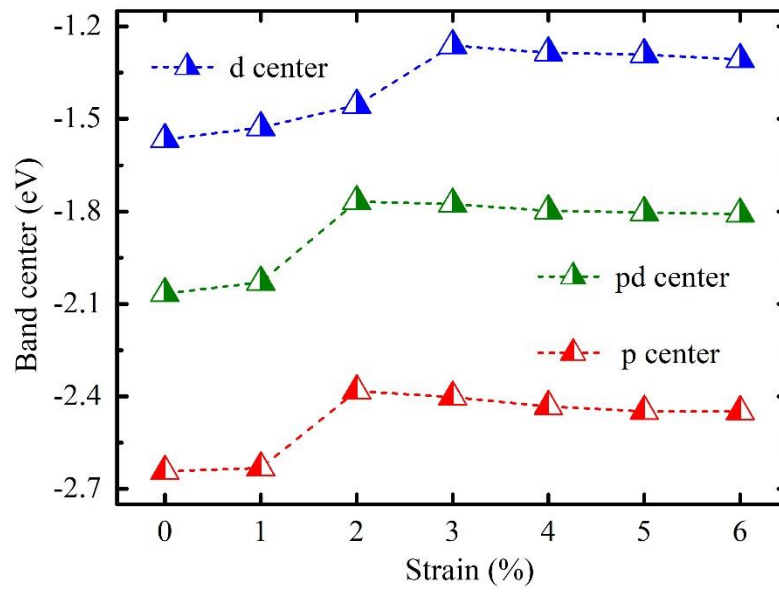
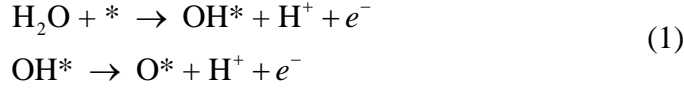
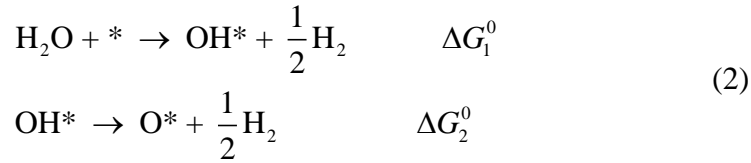


Figure S12 (Color online) The evolutions of the band center. The energy at the Fermi level was set to zero. In the process of stretching, the *d* band center plays a leading role for the evolutions of catalyst activity.

The surface Pourbaix diagrams of the equalitarian (0%) and strained (3%) states are constructed by plotting the thermodynamically most stable surface state under the relevant U_{SHE} and pH values. In our model, we assumed that the oxidation of water to OH^* and O^* on WB_4 lattice occurred through the following steps as suggested in ref [2]:



Under standard conditions, the free energy of $H^+ + e^-$ is equal to $1/2 H_2$. Therefore, the above equations can be rewritten as the following:



The Gibbs free energies of ΔG_1^0 and ΔG_2^0 are obtained by

$$\Delta G^0 = \Delta E + \Delta E_{ZPE} - T\Delta S \quad (3)$$

where ΔE is the energy difference from with and without adsorption. The values from $E_{ZPE} - T\Delta S$ are calculated on the basis of value from Table 1 of ref [3].

Equation (1) is dependent on the pH and potential U through the chemical potential of $H^+ + e^-$, while, equation (2) is not. To include the effects of pH and potential U , equation (3) can be rewritten as equation (4):

$$\begin{aligned} \Delta G_1 &= \Delta G_1^0 - eU_{SHE} - k_b T \ln 10 \times pH \\ \Delta G_2 &= \Delta G_2^0 - eU_{SHE} - k_b T \ln 10 \times pH \end{aligned} \quad (4)$$

The free energy change of OH^* and O^* termination can be expressed by

$$\begin{aligned} \Delta G_{OH^*} &= \Delta G_1 \\ \Delta G_{O^*} &= \Delta G_1 + \Delta G_2 \end{aligned}$$

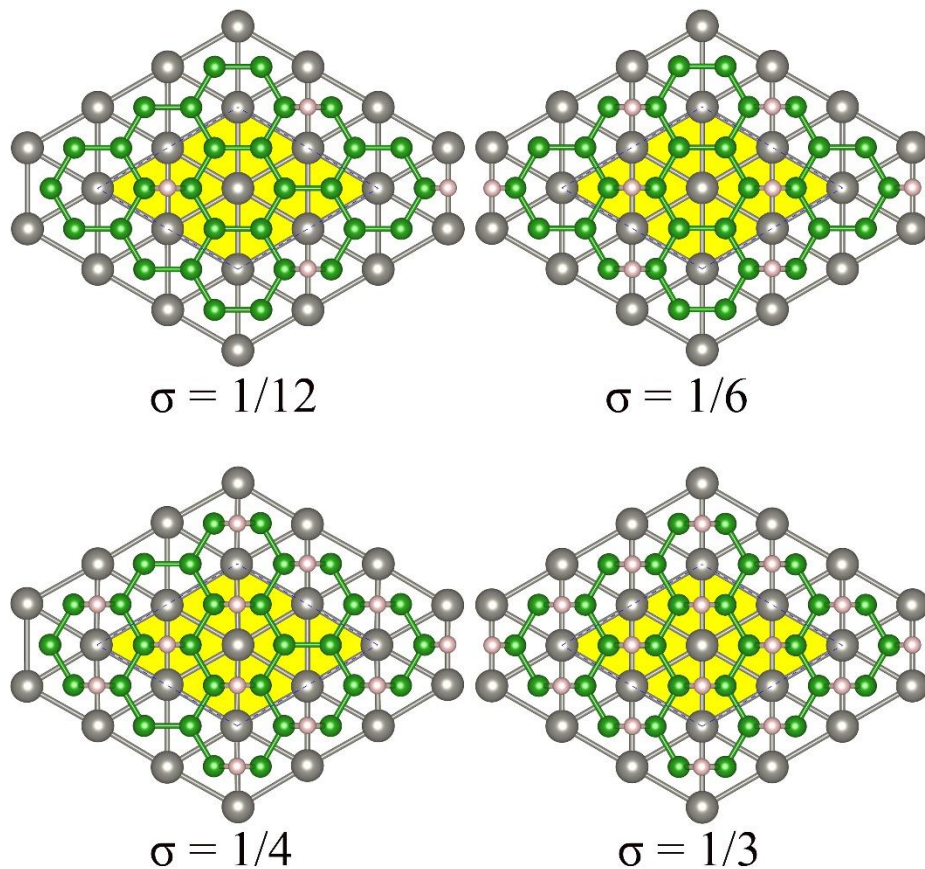


Figure S13 Schematic illustration of stable adsorption states with different hydrogen covering. The unit cell is indicated by the yellow shaded area.

References

- [1] Woods, H., Wawner, F., Fox, B.G., (1966) Tungsten diboride: preparation and structure, *Science*, 151, 75-75.
- [2] Hansen, H.A., Rossmeisl, J., Nørskov, J.K., (2008) Surface Pourbaix diagrams and oxygen reduction activity of Pt, Ag and Ni (111) surfaces studied by DFT, *Phys. Chem. Chem. Phys.*, 10, 3722-3730.

[3] Xu, H., Cheng, D., Cao, D., and Zeng, X.C. (2018). A universal principle for a rational design of single-atom electrocatalysts. *Nat. Catal.*, 1, 339-348.